ADVANCED FUNCTIONAL MATERIALS
www.afm-journal.de



# Highly Stretchable and Sensitive Strain Sensors Using Fragmentized Graphene Foam

*Yu Ra Jeong, Heun Park, Sang Woo Jin, Soo Yeong Hong, Sang-Soo Lee, and Jeong Sook Ha**

**Stretchable electronics have recently been extensively investigated for the development of highly advanced human-interactive devices. Here, a highly stretchable and sensitive strain sensor is fabricated based on the composite of fragmentized graphene foam (FGF) and polydimethylsiloxane (PDMS). A graphene foam (GF) is disintegrated into 200–300 μm sized fragments while maintaining its 3D structure by using a vortex mixer, forming a percolation network of the FGFs. The strain sensor shows high sensitivity with a gauge factor of 15 to 29, which is much higher compared to the GF/PDMS strain sensor with a gauge factor of 2.2. It is attributed to the great change in the contact resistance between FGFs over the large contact area, when stretched. In addition to the high sensitivity, the FGF/PDMS strain sensor exhibits high stretchability over 70% and high durability over 10 000 stretching-releasing cycles. When the sensor is attached to the human body, it functions as a health-monitoring device by detecting various human motions such as the bending of elbows and fingers in addition to the pulse of radial artery. Finally, by using the FGF, PDMS, and μ-LEDs, a stretchable touch sensor array is fabricated, thus demonstrating its potential application as an artificial skin.**

## 1. Introduction

As a result of the increasing demand for body attached electronic devices for health monitoring and biomedical applications, stretchable electronics have been rapidly developed in recent years. These devices are required to interact with the human body, and to act in a skin-like manner, deforming their shapes with external strain. In order to develop conventional portable electronic devices into body-attachable and wearable devices, stretchability beyond flexibility is required. For this purpose, a lot of research has been reported on the fabrication of stretchable devices in various fields such as electronic skins,[1–4] radiofrequency antennas,[5,6] light emitting diodes,[7–9] and energy storage devices.[10–14]

Above all, stretchable strain sensors have the advantages in a way that they can be used as practical wearable devices which can detect both large and subtle human motions when attached to the human body. As a wearable device, the strain sensor should be thin, light weight, and have a wide sensing range from a very small strain region such as a pulse (less than 1%) to a large strain region such as elbow bending (over 50%). In addition, the fabrication of the sensor must be simple and low-cost to ensure efficient production. Various materials such as carbon nanotubes,[15–17] graphene woven fabrics,[18] liquid-exfoliated graphene,[19,20] graphene–nanocellulose nanopapers,[21] carbon black,[22–24] metal nanoparticles,[25] and metal nanowires,[26,27] have been investigated to manufacture the strain sensors to satisfy these requirements.

Graphene foam (GF) with a macroporous network structure has achieved intense attention due to its large surface area and its excellent electrical and mechanical properties. It is used in diverse area including energy storage devices,[28,29] in addition to chemical and biological sensors.[30–32] In particular, when GF was combined with an elastomer such as polydimethylsiloxane (PDMS), it exhibited stable electrical and mechanical properties under various types of deformation, including stretching.[33] Current research on GF-based conductors have focused on fabricating a stretchable conductor that demonstrates constant resistance under external strain.[34–36] Pressure sensors and strain sensors that utilize the unique properties of the GF have also been reported,[37–39] but these GF-based strain sensors are only applicable for compressive and bending strain. When tensile strain is applied to the GF/PDMS composite, cracking and breaking of the graphene occurs, which causes the increase in resistance.[33] However, the change in the resistance ($\Delta R$) was not large enough to ensure the high sensitivity of the strain sensor. The sensitivity of the strain sensor is evaluated by a gauge factor, which is determined by the relationship between the relative resistance change ($\Delta R/R_0$) and the applied strain ($\varepsilon$). In order to improve the gauge factor of the GF/PDMS

Y. R. Jeong, H. Park, S. Y. Hong, Prof. J. S. Ha
Department of Chemical and Biological Engineering
Korea University
Seoul 136-701, South Korea
E-mail: jeongsha@korea.ac.kr
S. W. Jin, Prof. S.-S. Lee, Prof. J. S. Ha
KU-KIST Graduate School of Converging Science and Technology
Korea University
Seoul 136-701, South Korea
Prof. S.-S. Lee
Photo-Electronic Hybrids Research Center
Korea Institute of Science and Technology
Seoul 136-791, South Korea

DOI: 10.1002/adfm.201501000

composite as a strain sensor, a polyethylene terephthalate (PET) film was inserted as a substrate for GF.[40] Nonetheless, the GF-PET/PDMS could not be stretched and it still showed a low gauge factor (6.24) compared to that of strain sensors based on other materials such as silver nanowire (gauge factor ≈ 14),[26] graphene–nanocellulose nanopapers (gauge factor ≈ 7.1),[21] and liquid exfoliated graphene (gauge factor ≈ 35).[19]

In this study, we report on the facile fabrication of a highly stretchable and sensitive strain sensor by using a composite of GF and PDMS. In order to enhance the gauge factor, we fragmented the GF, which had been grown via chemical vapor deposition (CVD), into 200–300 μm sized fragments. This was performed using a vortex mixer with isopropyl alcohol (IPA). The fragmentized graphene foam (FGF) maintained the 3D structure of the GF. Following the rearrangement of the FGF by the drop-casting method, a 3D percolation network was formed and each FGF surface made contact with the adjacent FGF surfaces. The gauge factor of the strain sensor could be enhanced to achieve a value greater than 20 in result. This was because the applied strain resulted in a change in the contact resistance between the contacting FGFs over the large surface area. Our sensor demonstrated high stretchability over 70%, high durability over 10 000 stretching cycles, and a high gauge factor value from 15 to 29 depending on the FGF content and the maximum strain applied. Moreover, when the FGF/PDMS strain sensor was attached to the human body, it was capable of sensing various human motions such as the bending of elbows and fingers, in addition to a wrist pulse. Finally, as the FGF/PDMS composite could be manufactured in various shapes and sizes, we demonstrated an array of stretchable touch sensors composed of FGF, PDMS and μ-LEDs, which performed like an artificial skin.

## 2. Results and Discussion

Both the synthesis of the FGF and the fabrication of the strain sensor are illustrated in **Figure 1**a. A GF was grown on a 2 cm × 2 cm sized nickel foam template via the CVD technique. Following the etching of the nickel with hot HCl, the GF was immersed in a vial containing IPA solution. Subsequently, the GF was fragmentized with a vortex mixer for 20 min. Initially, the FGF exists in a dispersed state within the IPA, and then remains as a precipitate for 24 h, which enables the removal of a certain amount of IPA. Figure S1, Supporting Information, describes the corresponding states of the GF and FGF with the photographic images. The FGF/IPA solution was drop-cast using a micropipette onto a glass slide which was patterned in a rectangular shape (3 mm × 20 mm) with polyimide tape for the rearrangement of the FGF. The patterning of the electrodes with polyimide tape is very cost-effective and enables designing the electrodes in various shapes and sizes in a facile process.[26,41] The amount of the FGF that was used to fabricate the sensor could be controlled by the volume of the micropipette since the concentration of the FGF/IPA solution is made to be constant (4.9 mg $mL^{-1}$). After the removal of the remaining IPA in an oven, the polyimide tape was detached from the glass slide. Figure 1b shows the patterned FGF electrode, which was deposited onto the glass substrate. PDMS was poured onto the glass slide and a thin film of FGF/PDMS composite strain sensor was manufactured after curing and peeling off

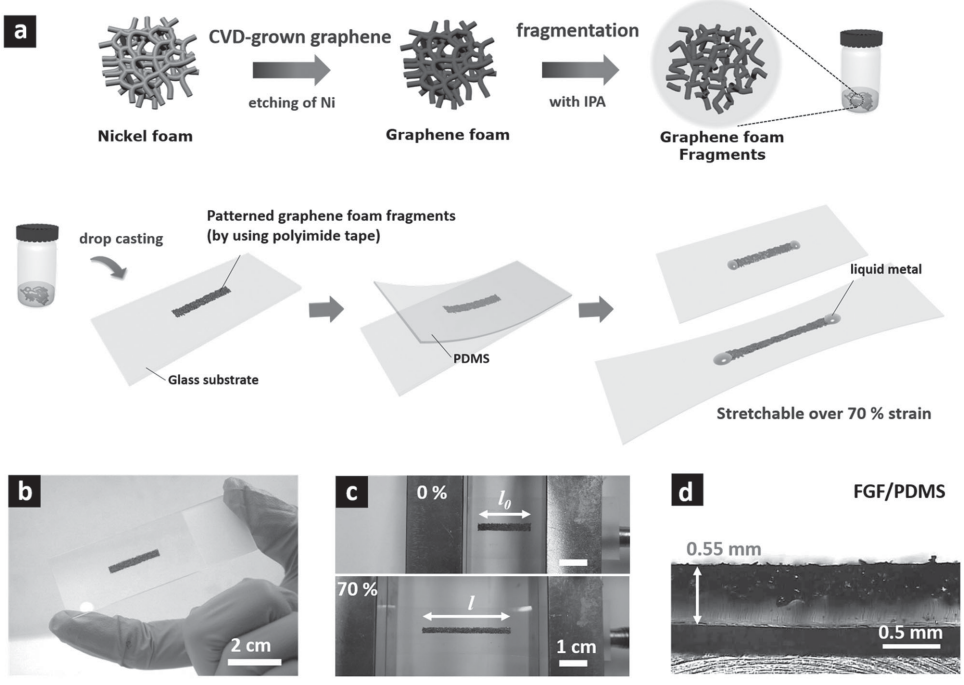


**Figure 1.** a) Schematic of the fabrication process of the FGF/PDMS strain sensors. b) An optical image of the FGFs deposited on a glass slide prior to pouring the PDMS. c) Optical images of the strain sensor before (top) and after (bottom) being stretched by 70%. Here, $l_0$ and $l$ are the length of the strain sensor before and after stretching by 70%, respectively. d) Cross-sectional image of the FGF/PDMS strain sensor.

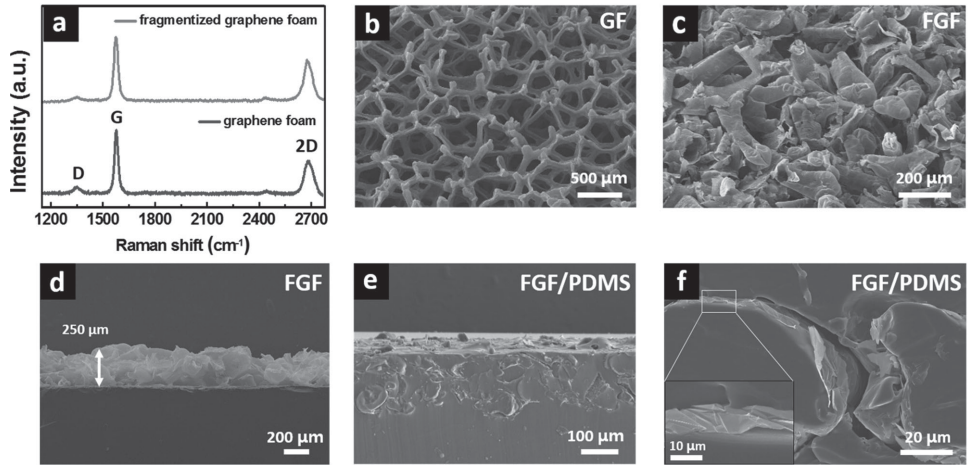


**Figure 2.** a) Raman spectra of GF (bottom) and FGF (top). b) SEM image of GF after etching of the nickel foam. SEM image of c) rearranged FGFs and d) the cross view of the patterned FGFs on the glass slide, respectively. e) Cross-sectional SEM image the strain sensor. f) Cross-sectional SEM images of the strain sensor where the PDMS was infiltrated into the hollow structure of the FGF.

the PDMS. To analyze the electrical properties of the sensor, we coated a few drops of liquid metal, Galinstan (eutectic alloy of 68.5% Ga, 21.5% In, and 10% Sn), onto both ends of the senor. When the sensor film was peeled off from the glass slide, a few pieces of the FGF on the top surface of the film were exposed to air, which facilitated the electrical wiring process (Figure S2, Supporting Information). The reason for using liquid metal rather than silver paste was that rigid silver paste could not endure a strain over 30%, and thus it interfered with the electrical signal of the sensor. In contrast, Galinstan retains high conductivity under various deformation and also generates low friction with the polymer surfaces when subjected to external strain.[16,42,43] In Figure 1c, the strain sensor was stretched by 70%, showing the high stretchability of the sensor. The applied strain is defined as follows

$$\text{Applied strain}(\%) = \frac{l - l_0}{l_0} \times 100 \quad (1)$$

where $l_0$ and $l$ are the lengths before and after the application of tensile strain, respectively, as indicated in Figure 1c, and the total length before stretching was fixed to be 3 cm. The thickness of the sensor was measured to be 0.55 mm in the cross-sectional optical image of Figure 1d.

**Figure 2**a shows the Raman spectra of the CVD grown GF and FGF obtained after the vortex mixer process. The ratio of the peak intensities between the 2D and G band ($I_{2D}/I_G$), and those between the D and G band ($I_D/I_G$) of the GF was 0.52 and 0.09, respectively, which indicates that multilayer graphene with a low defect density was grown via the CVD technique.[44] In addition, the $I_D/I_G$ value of the FGF was 0.06, which signifies that the lattice structure of the graphene is not affected by breaking the GF into fragments with the use of the vortex mixer. The morphology of the nickel-etched GF is shown in Figure 2b. The GF has a macroporous structure with pore sizes varying between 300 and 500 µm. Considering the 3D structure of the GF with a continuous network of branch shaped cylinders, the average length and diameter of the cylinders are estimated to be 280 and 67 µm, respectively. When the GF is being fragmentized by the vortex mixer, stress is applied to the GF. However, the graphene layer was neither randomly torn apart nor pulverized into small particles. Instead, it is observed that the graphene layer is torn from the vertices and that the FGF preserves the 3D structure of the GF (Figure 2c). Therefore, it can be deduced that the strain was not uniformly distributed in all parts, but it was focused on the vertices of the GF when external stress was applied. In recent works, the strain in the foam structure was calculated to be mainly concentrated on the joints of the GF using finite element analysis where the GF was expressed with a repetitive unit-cell model.[34,45] Moreover, the vertices of the GF are more rigid and brittle than the branches of the GF since the walls of the graphene thickens at the intersection of the branches,[46] thus enables them to fracture relatively easily. Figure 2d is a cross-sectional scanning electron microscope (SEM) image of the patterned and rearranged FGF percolation network, which was taken prior to the casting of the PDMS. The thickness of the patterned FGF electrode varies between 250 and 340 µm, depending on the volume of the micropipette, which was used to drop-cast the FGF/IPA onto the glass slide. The FGF pieces form a 3D conductive pathway while the individual FGF surfaces make contact with each other. The operating principle of the sensor is based on the change of the contact resistance between the FGF pieces according to the applied strain. Since the contact area between the FGF is significantly large, the gauge factor of the sensor can be considerably enlarged. The FGF/PDMS composite was produced by infiltrating PDMS into the hollow structure of the FGF. Figure 2e,f represent the cross-sectional SEM images of the fabricated strain sensor. The walls of the graphene enclosed the nickel template that was etched away. A closer look of the FGF/PDMS can be seen in Figure 2f, where the debonding of the graphene from the surrounding PDMS is observed. The inset clearly shows the inherent ripples of the graphene.

The electromechanical characteristics of the FGF/PDMS strain sensors are presented in **Figure 3**. For the measurements, two different strain sensors fabricated using 40 and 60 µL of FGF/IPA solutions were used, as indicated in each figure since both the sensitivity and the range of the strain sensing vary

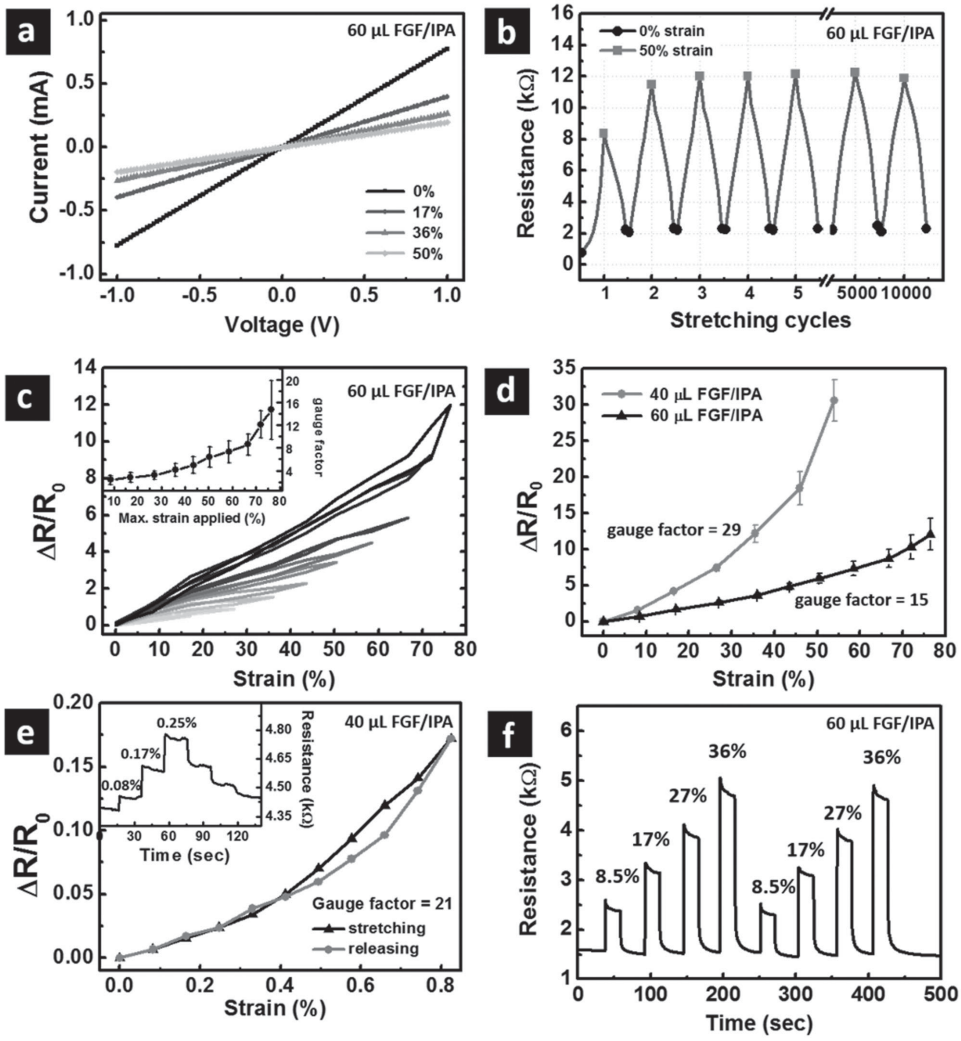


**Figure 3.** Electromechanical properties of the FGF/PDMS strain sensors. In each figure, the amount of FGF/IPA solution used for fabricating the sensor is indicated. a) Current–voltage curves of the strain sensors under various strain loadings. b) Electrical resistance change of the strain sensor with repeated cycles of stretching and releasing of 50% strain. After the first cycle, the sensor showed consistent resistance change during each cycle for over 10 000 cycles. c) The relative change in resistance versus strain curves of the sensor composed of 60 μL of FGF/IPA. The maximum applied strain increased from 8.5% to 77%. Each curve represents the corresponding maximum applied strain–resistance curve. The inset shows that the gauge factor increased according to the gradual increase of the maximum strain applied. d) The relative resistance change versus strain curves of the sensor with different content of FGF/IPA, i.e., 40 and 60 μL. e) The relative resistance change versus strain curves in the sensitive strain region of less than 1% strain, where the gauge factor exhibited the value of 21 ($R^2 = 0.944$). The inset shows a time–resistance curve for a stretching/releasing cycle with 0.25% strain. f) The time–resistance curve for repeated cycles.

with the amount of FGF. The strain sensor demonstrated linear current–voltage curves under various strains in Figure 3a, thus indicating the Ohmic behavior of the sensor. The resistance increased when a larger strain was applied. This was because the overlapping area between the adjacent FGF pieces decreased upon stretching, and the distance between the FGFs simultaneously increased. Figure 3b illustrates the change in the resistance with repeated cycles of stretching and releasing with 50% uniaxial strain. The resistance at zero strain, $R_0$, increased irreversibly during the initial stretching cycle, owing to the irreversible deformation of the composite and thus reducing of the number of the conductive pathways. The degree of irreversible deformation is proportional to the magnitude of the maximum strain applied. The increase in $R_0$ depending on the maximum strain is shown in Figure S3a, Supporting Information. The maximum applied strain is recorded as a strain history on resistance of the sensor, as commonly reported on researches in the field of conductive elastomer composite.[16,17,47,48] After the first cycle of stretching, $R_0$ retained its value for over 10 000 stretching cycles with the same applied strain, suggesting that the sensor has excellent durability and reliability. The relative change in resistance versus strain curve of Figure 3b is also presented in Figure S4, Supporting Information, which shows slight hysteresis due to the mechanical properties of PDMS.[49]

Figure 3c describes the change in the relative resistance with strain for various stretching cycles, which is the average value of the five different sensors with 60 μL FGF/IPA solution. While repeating two identical cycles, the maximum applied strain was

gradually increased from 8.5% to 77%. Here, the second cycle of each maximum strain cycle is shown in Figure 3c. The slope of the resistance versus strain curve increased as the maximum strain increased, where the slope represents the gauge factor. The gauge factor is defined as follows

$$\text{Gauge factor} = \frac{\Delta R / R_0}{\varepsilon} \quad (2)$$

where $\Delta R$, $R_0$, and $\varepsilon$ represent the change of resistance, the resistance at 0% strain, and the applied strain, respectively. The inset is the average value of the gauge factors with standard deviation of the five sensors, which depicts the monotonic increase of the gauge factor from 2.4 to 15 in accordance with the increase of the maximum applied strain from 8.5% to 77%. When a greater value of maximum strain is applied, it leads to an increase in the gauge factor. This is because the effect of the decreasing percolation network becomes more crucial with fewer conductive pathways.[20] As confirmed in Figure 3b, once the $R_0$ increases, it retains a constant value during further stretching cycles owing to the strain history. Additionally, it can be inferred that once the sensor is stretched over 70% stain, the gauge factor would maintain its large value even for the strain lower than 70%. Figure S3b, Supporting Information, shows that the gauge factor maintained a higher magnitude after increasing the maximum strain from 55% to 78%, when the sensor was repeatedly stretched to 55% strain over 2000 stretching cycles. The variation in the gauge factor, indicated as error bars, among five different sensors (inset of Figure 3c) is mainly attributed to the drop-casting method which is not delicate enough considering the relatively large size of the FGF (average diameter and length of 67 and 280 μm, respectively) compared to other nanomaterials. The variation of the performance among five different sensors with the same amount of FGF is shown in Figure S5, Supporting Information, with two extreme cases.

The fact that the gauge factor is affected by the number of conductive pathways suggests that it be tuned by adjusting $R_0$ with the amount of FGF used. To vary the initial resistance, we controlled the volume of the micropipette to be 40 and 60 μL, which was used for drop-casting the FGF/IPA onto the patterned glass slide, while the concentration of the solution was fixed to 4.9 mg $mL^{-1}$. The average initial resistance of the sensor with 40 and 60 μL FGF/IPA solutions was 1.8 and 0.47 kΩ, respectively. The resistance declined as the FGF contents increased, because more conductive pathways were generated with a larger overlapping area between the FGFs. Figure 3d shows the change in the normalized resistance plotted against the strain curve, with different amounts of FGF used. At each amount of FGF, the average relative resistance and the standard deviation of the sensor were calculated by measuring the resistance of five different sensors to confirm the reproducibility. The strain sensors with 60 μL FGF/IPA solution exhibited linear behavior in the strain–resistance curve, with the gauge factors of 15 ($R^2$ = 0.959) to 77% strain. As expected, with a smaller amount of FGF, a higher value of the gauge factor was obtained. When subjected to a maximum strain of 70%, the sensor with a relatively small amount of FGF (40 μL) showed linear change in resistance to 36% strain ($R^2$ = 0.983) with a gauge factor of 29. It also showed stable electrical performance to 54% strain. For comparison, we examined electromechanical characteristic of a GF/PDMS composite sensor, where the size of the electrode was equal to that of our FGF/PDMS strain sensor and the amount of the GF used approximately corresponded to 50 μL of the FGF/IPA. (Figure S6, Supporting Information) The GF/PDMS composite sensor was repeatedly stretched to 60% strain to stabilize the change of the resistance.[33] In Figure S6b, Supporting Information, the relative resistance ($\Delta R/R_0$) at 60% strain was only 0.86 and the gauge factor in the linear range (to 30% strain) was 2.2. These results confirm that the FGF/PDMS strain sensor achieved higher sensitivity than that of GF/PDMS sensor via fragmentation of GF, as we expected.

In addition to their use in the high strain region, the FGF/PDMS strain sensors can also be used in the low strain region less than 1%. Figure 3e demonstrates the change in resistance in response to 0.083% increase in strain with the gauge factor of 21 ($R^2$ = 0.944), and the inset shows the time–resistance curve of the stretching/releasing cycle with 0.25% strain. In Figure 3f, the sensor showed an identical resistance response to repeated stretching cycles with a gradual increase of strain from 8.5% to 36%, thus indicating the reliability of the sensor. The sharp overshoots are tensile stress-relaxation for the applied strain, which can be attributed to the viscoelasticity of the PDMS composite.[50,51]

For a more precise understanding of the operating principle of the sensor, the deformation of the FGF/PDMS composite under different strains is demonstrated in **Figure 4**. Figure 4a shows the sequentially captured optical images of the FGF/PDMS film with increasing strain. The film was fabricated by using a very small amount of FGF. When the FGF/PDMS film was subjected to an uniaxial strain, both the transparent PDMS portion and the FGF/PDMS fragments underwent mechanical deformation such as shape deformation, and the FGF/PDMS was reorientated in the direction of the applied strain.[16] Within the images, there is no noticeable disconnection of

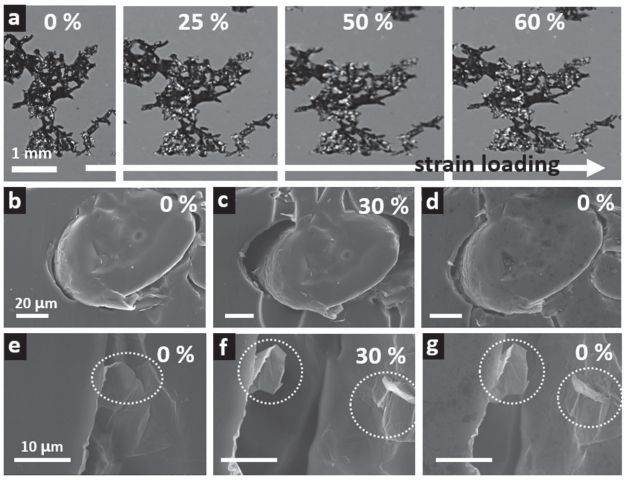


**Figure 4.** Mechanical deformation of the FGF/PDMS composite. a) Series of photographic images of the FGF/PDMS composite being stretched from 0% to 60%. A small number of FGF pieces undergo mechanical deformation during stretching. b–g) Cross-sectional SEM images of the strain sensor captured in unloaded states (b,e), 30% stretched states (c,f), and released states (d,g).

the graphene observed. Figure 4b–g show the cross-sectional SEM images of the fabricated strain sensor, where the sensor sequentially underwent initial stretching to 30% and releasing to 0%. In Figure 4b–d, the outer surrounding PDMS matrix was stretched but a relatively small strain was transferred to the inner PDMS which infiltrated into the FGF. This is attributed to the energy absorption in the composite due to the detachment of the graphene from the surrounding PDMS with the moderate interfacial adhesion.[52,53] When the sensor was released back from 30% to 0% strain (Figure 4d), the distance between the graphene walls and the outer PDMS increased compared to the original unloaded state (Figure 4d) due to the hysteresis of the elastomer.[49] This has resulted in the irreversible increase of the $R_0$ value during the initial stretching, which was observed in our measurement of Figure 3b. The separation between the FGF and the PDMS matrix facilitates the change in the orientation and position of the FGF. The debonding of the graphene also enables the generation of less damage to the graphene in further repetitive stretching cycles, which contributes to the high durability of the strain sensor. Figure S7, Supporting Information, shows the deformation of the FGF/PDMS when the individual FGF pieces contact with adjacent FGFs. In this case, the FGFs were connected to the permeated PDMS and these PDMS connections were stretched when strain was applied to the sensor. Figure 4e–g present the breaking of the graphene layer during the initial stretching of the sensor by 30%. The graphene was torn in the direction of applied strain (Figure 4f) and remained disconnected even when the strain was released back to 0% (Figure 4g), which is consistent with the increase in the $R_0$ value during the initial stretching measured in Figure 3b. Here the circles indicate the graphene layer torn apart.

In order to evaluate the FGF/PDMS strain sensor as a wearable device, it was attached to the human body to detect various biosignals. Since the sensor was as thin as 0.55 mm, it was simply attached to the human body using an adhesive silicone elastomer, Silbione (4717 A/B, Bluestar Silicones, USA).[54] **Figure 5**a shows the pulse signal of the radial artery from the wrist. Significant information of the arterial wall can be obtained from the arterial pulse waveforms such as stiffness of an aortic system as well as the velocity and pressure of the pulse. The waveform consists of a forward arterial wave and reflected waves from the periphery.[55] In the inset of Figure 5, which is a magnified view of a pulse wave, three distinguishable peaks can be observed; each corresponds with the incident forward wave ($P_1$), reflected waveforms of late systolic wave ($P_2$), and early diastolic wave ($P_3$).[55] Figure S8, Supporting Information, shows magnified view of other waveforms shown in Figure 5a, which exhibit similar characteristics of the radial artery pulse. Figure 5b,c illustrate the detection of elbow and finger bending, respectively, following the placement of the sensor on the joints of the body. Compared to the change in length between folded and unfolded state of the elbow and the finger (each for 40% and 25% increase, respectively), the change in relative resistance shown in Figure 5b,c is small. This is due to the soft adhesive elastomer medium between human skin and the sensor. As the modulus of the Silbione is extremely low (≈3.0 kPa),[54] it can be deduced that relatively small strain have been transferred to the FGF/PDMS strain sensor. We compared the change in the relative resistance of an identical strain sensor with and without the use of Silbione in Figure S9, Supporting Information. As a result, the change of the relative resistance is much smaller in the case of Silbione applied sensor compared with the case that used the polyimide tape to attach the sensor onto the skin. However, without using

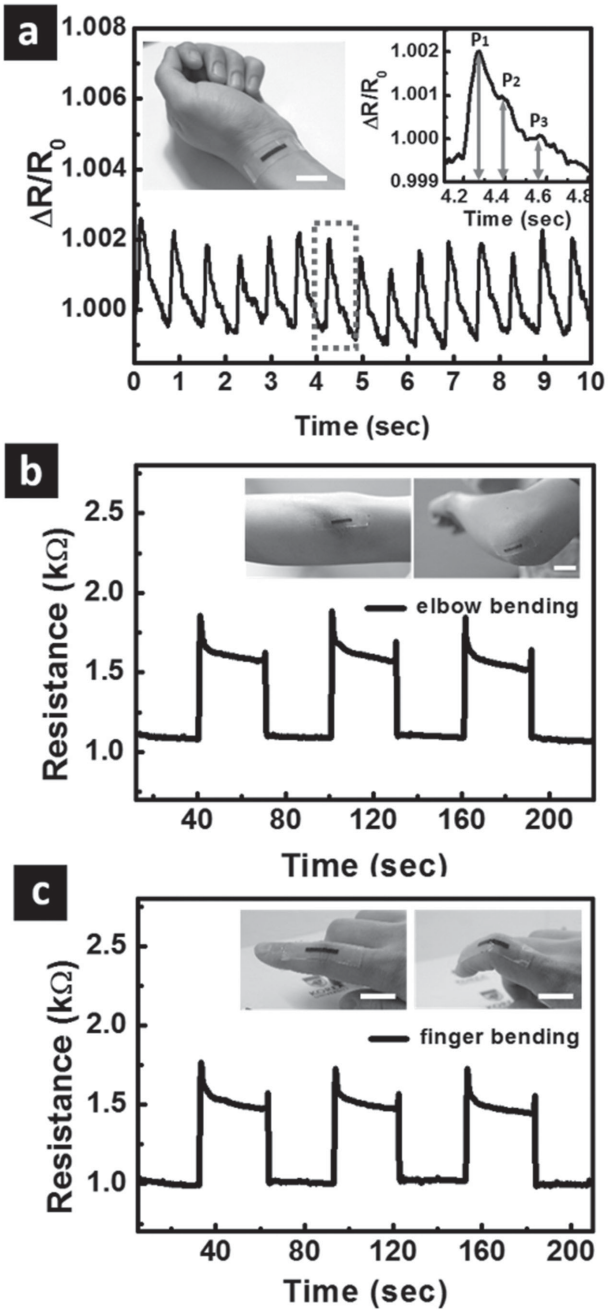


**Figure 5.** Detection of bio-signals with the FGF/PDMS strain sensor attached to the human body using Silbione. a) The relative resistance change of the sensor in response to the pulse of radial artery from the wrist. The inset shows the region in the dashed box. Here, 40 μL of FGF/IPA was used. Resistance change with b) elbow and c) finger bending, respectively, where 60 μL of FGF/IPA was used. Here the scale bars correspond to 2 mm.

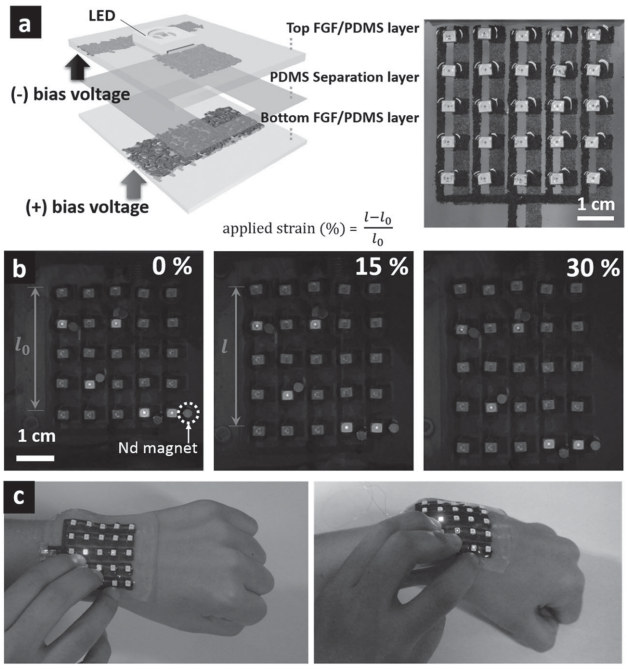


**Figure 6.** a) A schematic of the stretchable touch sensor array (STS) based on the FGF/PDMS composite and μ-LEDs (left) and a corresponding optical image of the fabricated STS (right). b) Series of photograph images of the STS being stretched to 30%, while the LED lights are selectively switched on by clipping the touch pads using neodymium magnets. Here, $l_0$ and $l$ are the length of STS before and after stretching, respectively. The applied strain is defined as, applied strain (%) = $(l–l_0)/l_0 \times 100$. c) Photographic images of the STS attached to the wrist before (left) and after (right) bending, respectively.

Silbione it was difficult to fix the sensor during joint movements due to a generation of high stress according to the high strain made in FGF/PDMS. Moreover it is very uncomfortable for the skin and arm because the skin is severely pressed by polyimide tape and the sensor, which also lead to an inaccurate strain measurement (34% rather than 40% strain) as shown in Figure S9e, Supporting Information. Although using Silbione limits the detection of the actual strain value, it helps application of the strain sensor to be used as a wearable device.

Since the FGF/PDMS composite can be fabricated in various shapes and sizes via a simple process, we considered that it has a potential as a stretchable conductor. For further applications, we fabricated an array of 5 × 5 stretchable touch sensors composed of the patterned FGF, PDMS, and μ-LEDs (**Figure 6**a). The stretchable touch sensor (STS) array is an on/off type touch sensor, which activates the μ-LEDs when the touch pads are pressed. The STS consists of three different layers; the top layer has patterned FGF electrodes that are positioned next to the square touch pads with the μ-LEDs, whose components are all embedded in the PDMS. The middle layer is a thin PDMS film, which functions as a separator between the top and the bottom layer with the exception of square holes, which are perforated below the touch pad. The bottom layer consists of the PDMS and patterned FGF electrodes, which have the same width as the touch pad. Finally, the three layers are aligned and combined together. Figure S10, Supporting Information, shows the patterned FGF electrodes and the μ-LEDs prior to the casting of the PDMS. The total size of the STS was 44 cm × 54 cm, and the final thickness of the STS was approximately 2 mm.

Figure 6b demonstrates the successful operation of the fabricated STS via lighting the μ-LEDs regardless the stretching of the STS up-to 30%. The $l_0$ and $l$ are the lengths indicated in Figure 6b and the applied strain is defined as given in the figure. The μ-LED lights were switched on when each touch pad was clipped by two neodymium magnets that were placed on the top and the bottom layer of the STS. In Supporting Movie S1, the repetitive stretching and releasing of the STS by 30% uniaxial strain was performed. Upon stretching, the intensity of the LED lights was slightly reduced according to the applied strain due to the increase in the resistance of the FGF/PDMS composite. The light intensity at zero strain also decreased after the first stretching cycle owing to the irreversible increase in $R_0$. However, it changed consistently with the applied strain in further stretching cycles, which indicates the reversible operation of the STS. Such variance in the intensity of the lights with stretching cycles corresponds with the result of Figure 3b. In Figure 6c, it is shown that the device was attached to the wrist and the LED lights were selectively switched on in both unstrained (left) and strained (right) states. These results demonstrate that the FGF/PDMS-based STS can be used as an artificial skin and has the potential to be applied in a wide range of stretchable devices.

## 3. Conclusion

In this study, we have demonstrated the successful performance of a highly stretchable and sensitive strain sensor fabricated using a composite of FGF and PDMS. The GF was fragmentized while maintaining a 3D structure and the surfaces of the adjacent FGFs had contact with each other forming 3D percolation networks. The fabricated sensors demonstrated high stretchability over 70% strain and high durability over 10 000 stretching cycles with a gauge factor in the range of 15–29 depending on the maximum strain applied and the FGF content. The enhanced gauge factor compared to the GF/PDMS strain sensor is attributed to the increase in the change of the resistance with applied strain owing to the large contact area between adjacent FGFs, whose effect was apparently large compared to partial breaking and cracking of the GF when stretched. The FGF/PDMS strain sensors were also capable of sensing sensitive strain regions with less than 1% strain. The body-attached strain sensor showed successful detection of biosignals such as a wrist pulse, and the bending of elbows and fingers; thus demonstrating its potential application as a wearable bio-sensor. Moreover, an array of stretchable touch sensors could be fabricated by combining μ-LEDs with the FGF/PDMS composite, and thus it could work like an artificial skin.

The fragmentation process has a potential to be applied in other materials which have porous, mesh or bush type 3D structure. By reorganizing the fragments, different mechanical and electrical characteristics could be obtained due to the enlarged surface contact areas. Those properties can be utilized in various gas sensors and biosensors as well as strain or pressure sensors.

## 4. Experimental Section

*Fabrication of GF and FGF*: The multilayer graphene was grown on a nickel foam template (Goodfellow Cambridge Ltd, England. (2 cm × 2 cm, 1.6 mm thickness, 95% porosity, 0.45 g $cm^{-3}$ bulk density)) via the CVD method. The nickel foam was placed into the middle of the quartz tube and a flow of Ar and $H_2$ gas ($Ar/H_2$ = 500/200 sccm) was supplied to the tube under ambient pressure. The temperature increased to 1000 °C for a period of 20 min and annealing was conducted for 10 min in order to clean the surfaces.[33] The graphene was synthesized by introducing $CH_4$ (30 sccm) into the quartz tube for 20 min at a temperature of 1000 °C. On completion of the growth, the quartz tube was rapidly cooled to room temperature. To remove the nickel template, the graphene/nickel foam was immersed into 3 M of HCl at a temperature of 80 °C for 24 h. The GF (with a dimension of 2 cm × 2 cm, 1.56 mg) was placed into a vial with 10 g of IPA. The GF was subsequently fragmentized by operating a vortex mixer (Scientific Industries, INC., G-560) at an intensity of 7 for 20 min. Precipitation of the FGF was conducted for one day and the IPA was removed; leaving 0.4 g of FGF/IPA.

*Fabrication of Thin Film FGF/PDMS Strain Sensors*: A pattern with a size of 20 mm × 3 mm was formed on a glass slide (76 mm × 26 mm) by using polyimide tape. The FGF/IPA (4.9 mg $mL^{-1}$) was drop-cast onto the patterned glass slide with a micropipette. The volumes of FGF/IPA used were 40 and 60 µL. After the removal of the IPA in a 65 °C oven, liquid PDMS (Sylgard 184, Dow Corning) was poured onto the glass slide in a petri dish and it was cured at 65 °C for 1 h. After curing, the FGF/PDMS composite film was peeled off from the glass slide and Galinstan (68.5% Ga, 21.5% In, and 10% Sn; Rotometals) was casted onto both ends of the FGF electrode for electrical characterization.

*Fabrication of Stretchable Touch Sensor Array*: In order to fabricate the top and bottom layer of the STS, a pattern was formed on a glass substrate (147 mm × 147 mm) with polyimide tape. Five parallel electrodes were patterned for each layer. The width was 1.5 mm for the top layer and 3 mm for the bottom layer, respectively. For the top layer, a 5 × 5 array of square touch pads (3 mm × 3 mm) was patterned additionally. The polyimide tape was removed after the drop-casting of the FGF/IPA and the evaporation of the IPA. Twenty-five µ-LEDs (3.2 mm × 2.8 mm) were placed between the electrodes and each touch pad (in the same pole direction). Liquid PDMS (15 g) was poured onto the glass substrate and it was subsequently placed into a vacuum desiccator for 20 min in order to fully infiltrate the PDMS into the FGF. The PDMS was cured for 1 h and subsequently peeled off from the glass substrate. For the middle layer, a thin PDMS film was prepared and 25 square holes were perforated in order to be aligned with the touch pads of the top layer. Following the fabrication of the three layers, they were assembled and aligned so that the touch pads could contact the electrodes of the bottom layer when pressed. A 9 V commercial battery was used to light up the µ-LEDs and the negative and positive ends of the battery were connected to the top and bottom layer, respectively.

*Characterization*: To analyze the quality of the synthesized GF and FGF, Raman spectroscopy (custom built with a wavelength of 532 nm and power of 50 mW) was performed. The morphology of the GF and FGF/PDMS composite was investigated by SEM (Hitachi S-4800) and a camera (Cannon, EOS 7D) with a macro lens (Cannon, EF 100 mm f/2.8L Macro IS USM). The electromechanical characterization of the strain sensor was performed by mounting the sensor onto a custom-built stretching stage and by controlling the position with computer software (PMC-1HS, Autonics Corp., Korea). The electrical signal was measured by a probe station (MS Tech, 8000).

## Supporting Information

Supporting Information is available from the Wiley Online Library or from the author.

## Acknowledgements

This work was supported by the National Research Foundation of Korea (NRF) grant funded by the Korea government (MEST) (Grant No. NRF-2013R1A2A1A01016165). The authors also thank the KU-KIST Graduate School Program of Korea University, Korea.

Received: March 13, 2015
Revised: May 1, 2015
Published online: May 27, 2015

[1] T. Sekitani, Y. Noguchi, K. Hata, T. Fukushima, T. Aida, T. Someya, *Science* **2008**, *321*, 1468.
[2] D.-H. Kim, N. Lu, R. Ma, Y.-S. Kim, R.-H. Kim, S. Wang, J. Wu, S. M. Won, H. Tao, A. Islam, K. J. Yu, T.-i. Kim, R. Chowdhury, M. Ying, L. Xu, M. Li, H.-J. Chung, H. Keum, M. McCormick, P. Liu, Y.-W. Zhang, F. G. Omenetto, Y. Huang, T. Coleman, J. A. Rogers, *Science* **2011**, *333*, 838.
[3] D.-H. Kim, Y.-S. Kim, J. Wu, Z. Liu, J. Song, H.-S. Kim, Y. Y. Huang, K.-C. Hwang, J. A. Rogers, *Adv. Mater.* **2009**, *21*, 3703.
[4] S. Park, H. Kim, M. Vosgueritchian, S. Cheon, H. Kim, J. H. Koo, T. R. Kim, S. Lee, G. Schwartz, H. Chang, Z. Bao, *Adv. Mater.* **2014**, *26*, 7324.
[5] M. Kubo, X. Li, C. Kim, M. Hashimoto, B. J. Wiley, D. Ham, G. M. Whitesides, *Adv. Mater.* **2010**, *22*, 2749.
[6] L. Song, A. C. Myers, J. J. Adams, Y. Zhu, *ACS Appl. Mater. Interfaces* **2014**, *6*, 4248.
[7] R.-H. Kim, M.-H. Bae, D. G. Kim, H. Cheng, B. H. Kim, D.-H. Kim, M. Li, J. Wu, F. Du, H.-S. Kim, S. Kim, D. Estrada, S. W. Hong, Y. Huang, E. Pop, J. A. Rogers, *Nano Lett.* **2011**, *11*, 3881.
[8] J. Liang, L. Li, K. Tong, Z. Ren, W. Hu, X. Niu, Y. Chen, Q. Pei, *ACS Nano* **2014**, *8*, 1590.
[9] M. S. White, M. Kaltenbrunner, E. D. Glowacki, K. Gutnichenko, G. Kettlgruber, I. Graz, S. Aazou, C. Ulbricht, D. A. M. Egbe, M. C. Miron, Z. Major, M. C. Scharber, T. Sekitani, T. Someya, S. Bauer, N. S. Sariciftci, *Nat. Photonics* **2013**, *7*, 811.
[10] C. Yu, C. Masarapu, J. Rong, B. Wei, H. Jiang, *Adv. Mater.* **2009**, *21*, 4793.
[11] L. Hu, M. Pasta, F. L. Mantia, L. Cui, S. Jeong, H. D. Deshazer, J. W. Choi, S. M. Han, Y. Cui, *Nano Lett.* **2010**, *10*, 708.
[12] S. Y. Hong, J. Yoon, S. W. Jin, Y. Lim, S.-J. Lee, G. Zi, J. S. Ha, *ACS Nano* **2014**, *8*, 8844.
[13] B. Y. Lim, J. Yoon, J. Yun, D. Kim, S. Y. Hong, S.-J. Lee, G. Zi, J. S. Ha, *ACS Nano* **2014**, *8*, 11639.
[14] D. Kim, G. Shin, Y. J. Kang, W. Kim, J. S. Ha, *ACS Nano* **2013**, *7*, 7975.
[15] T. Yamada, Y. Hayamizu, Y. Yamamoto, Y. Yomogida, A. Izadi-Najafabadi, D. N. Futaba, K. Hata, *Nat. Nanotechnol.* **2011**, *6*, 296.
[16] D. J. Lipomi, M. Vosgueritchian, B. C. Tee, S. L. Hellstrom, J. A. Lee, C. H. Fox, Z. Bao, *Nat. Nanotechnol.* **2011**, *6*, 788.
[17] L. Cai, J. Li, P. Luan, H. Dong, D. Zhao, Q. Zhang, X. Zhang, M. Tu, Q. Zeng, W. Zhou, S. Xie, *Adv. Funct. Mater.* **2012**, *22*, 5238.
[18] X. Li, P. Sun, L. Fan, M. Zhu, K. Wang, M. Zhong, J. Wei, D. Wu, Y. Cheng, H. Zhu, *Sci. Rep.* **2012**, *2*.
[19] C. S. Boland, U. Khan, C. Backes, A. O'Neill, J. McCauley, S. Duane, R. Shanker, Y. Liu, I. Jurewicz, A. B. Dalton, J. N. Coleman, *ACS Nano* **2014**, *8*, 8819.
[20] M. Hempel, D. Nezich, J. Kong, M. Hofmann, *Nano Lett.* **2012**, *12*, 5714.
[21] C. Yan, J. Wang, W. Kang, M. Cui, X. Wang, C. Y. Foo, K. J. Chee, P. S. Lee, *Adv. Mater.* **2014**, *26*, 2022.
[22] N. Lu, C. Lu, S. Yang, J. Rogers, *Adv. Funct. Mater.* **2012**, *22*, 4044.
[23] C. Mattmann, F. Clemens, G. Tröster, *Sensors* **2008**, *8*, 3719.

[24] J. T. Muth, D. M. Vogt, R. L. Truby, Y. Mengüç, D. B. Kolesky, R. J. Wood, J. A. Lewis, *Adv. Mater.* **2014**, *26*, 6307.
[25] J. Lee, S. Kim, J. Lee, D. Yang, B. C. Park, S. Ryu, I. Park, *Nanoscale* **2014**, *6*, 11932.
[26] M. Amjadi, A. Pichitpajongkit, S. Lee, S. Ryu, I. Park, *ACS Nano* **2014**, *8*, 5154.
[27] S. Yao, Y. Zhu, *Nanoscale* **2014**, *6*, 2345.
[28] H. Ji, L. Zhang, M. T. Pettes, H. Li, S. Chen, L. Shi, R. Piner, R. S. Ruoff, *Nano Lett.* **2012**, *12*, 2446.
[29] Y. S. Moon, D. Kim, G. Lee, S. Y. Hong, K. K. Kim, S. M. Park, J. S. Ha, *Carbon* **2015**, *81*, 29.
[30] F. Yavari, Z. Chen, A. V. Thomas, W. Ren, H.-M. Cheng, N. Koratkar, *Sci. Rep.* **2011**, *1*, 166.
[31] X.-C. Dong, H. Xu, X.-W. Wang, Y.-X. Huang, M. B. Chan-Park, H. Zhang, L.-H. Wang, W. Huang, P. Chen, *ACS Nano* **2012**, *6*, 3206.
[32] H. Y. Yue, S. Huang, J. Chang, C. Heo, F. Yao, S. Adhikari, F. Gunes, L. C. Liu, T. H. Lee, E. S. Oh, B. Li, J. J. Zhang, T. Q. Huy, N. V. Luan, Y. H. Lee, *ACS Nano* **2014**, *8*, 1639.
[33] Z. Chen, W. Ren, L. Gao, B. Liu, S. Pei, H.-M. Cheng, *Nat. Mater.* **2011**, *10*, 424.
[34] M. Chen, L. Zhang, S. Duan, S. Jing, H. Jiang, C. Li, *Adv. Funct. Mater.* **2014**, *24*, 7548.
[35] C. Wu, L. Fang, X. Huang, P. Jiang, *ACS Appl. Mater. Interfaces* **2014**, *6*, 21026.
[36] M. Chen, S. Duan, L. Zhang, Z. Wang, C. Li, *Chem. Commun.* **2015**, *51*, 3169.
[37] J. Kuang, L. Liu, Y. Gao, D. Zhou, Z. Chen, B. Han, Z. Zhang, *Nanoscale* **2013**, *5*, 12171.
[38] H. B. Yao, J. Ge, C. F. Wang, X. Wang, W. Hu, Z. J. Zheng, Y. Ni, S. H. Yu, *Adv. Mater.* **2013**, *25*, 6692.
[39] Y. A. Samad, Y. Li, A. Schiffer, S. M. Alhassan, K. Liao, *Small* **2015**, DOI: 10.1002/smll.201403532.
[40] R. Xu, Y. Lu, C. Jiang, J. Chen, P. Mao, G. Gao, L. Zhang, S. Wu, *ACS Appl. Mater. Interfaces* **2014**, *6*, 13455.
[41] S. K. Mohanty, J. Warrick, J. Gorski, D. J. Beebe, *Electrophoresis* **2009**, *30*, 1470.
[42] L. Tingyi, P. Sen, K. Chang-Jin, *J. Microelectromech. Syst.* **2012**, *21*, 443.
[43] M. D. Dickey, R. C. Chiechi, R. J. Larsen, E. A. Weiss, D. A. Weitz, G. M. Whitesides, *Adv. Funct. Mater.* **2008**, *18*, 1097.
[44] A. C. Ferrari, J. C. Meyer, V. Scardaci, C. Casiraghi, M. Lazzeri, F. Mauri, S. Piscanec, D. Jiang, K. S. Novoselov, S. Roth, A. K. Geim, *Phys. Rev. Lett.* **2006**, *97*, 187401.
[45] Y. Kwon, R. Cooke, C. Park, *Mater. Sci. Eng., A* **2003**, *343*, 63.
[46] A. Nieto, B. Boesl, A. Agarwal, *Carbon* **2015**, *85*, 299.
[47] L. Cai, L. Song, P. Luan, Q. Zhang, N. Zhang, Q. Gao, D. Zhao, X. Zhang, M. Tu, F. Yang, W. Zhou, Q. Fan, J. Luo, W. Zhou, P. M. Ajayan, S. Xie, *Sci. Rep.* **2013**, *3*, 3048
[48] U.-H. Shin, D.-W. Jeong, S.-M. Park, S.-H. Kim, H. W. Lee, J.-M. Kim, *Carbon* **2014**, *80*, 396.
[49] T. K. Kim, J. K. Kim, O. C. Jeong, *Microelectron. Eng.* **2011**, *88*, 1982.
[50] S. Wang, P. Wang, T. Ding, *Polym. Compos.* **2011**, *32*, 29.
[51] F. Ehrburger-Dolle, I. Morfin, F. Bley, F. Livet, G. Heinrich, L. Piché, M. Sutton, *J. Polym. Sci., Part B: Polym. Phys.* **2014**, *52*, 647.
[52] J. Jia, X. Sun, X. Lin, X. Shen, Y.-W. Mai, J.-K. Kim, *ACS Nano* **2014**, *8*, 5774.
[53] S. Scharfenberg, N. Mansukhani, C. Chialvo, R. L. Weaver, N. Mason, *Appl. Phys. Lett.* **2012**, *100*, 021910.
[54] K.-I. Jang, S. Y. Han, S. Xu, K. E. Mathewson, Y. Zhang, J.-W. Jeong, G.-T. Kim, R. C. Webb, J. W. Lee, T. J. Dawidczyk, R. H. Kim, Y. M. Song, W.-H. Yeo, S. Kim, H. Cheng, S. I. Rhee, J. Chung, B. Kim, H. U. Chung, D. Lee, Y. Yang, M. Cho, J. G. Gaspar, R. Carbonari, M. Fabiani, G. Gratton, Y. Huang, J. A. Rogers, *Nat. Commun.* **2014**, *5*, 4779.
[55] M. F. O'Rourke, A. Pauca, X.-J. Jiang, *Br. J. Clin. Pharmacol.* **2001**, *51*, 507.